

pubs.acs.org/IECR Article

# Size-Dependent Activity of Iron Nanoparticles in Both Thermal and Plasma Driven Catalytic Ammonia Decomposition

Genwei Chen, Jing Qu, Pohlee Cheah, Dongmei Cao, Yongfeng Zhao,\* and Yizhi Xiang\*



Cite This: Ind. Eng. Chem. Res. 2022, 61, 11436-11443



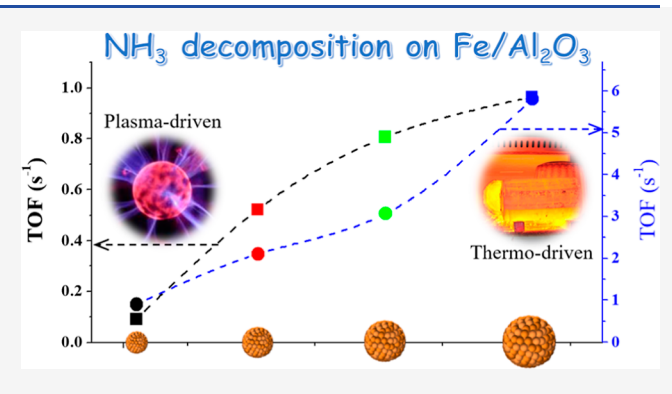
**ACCESS** I

III Metrics & More

Article Recommendations

s Supporting Information

**ABSTRACT:** Water-dispersible Fe $_3$ O $_4$  nanoparticles with diameters of 4.2  $\pm$  0.6, 6.1  $\pm$  0.8, 8.1  $\pm$  1, and 10.4  $\pm$  1 nm were prepared through the polyol method and employed as the precursors of Fe $_3$ O $_4$ /Al $_2$ O $_3$  catalysts to study the size-dependent activity. We identified that the activity of the catalysts in NH $_3$  decomposition (driven by both thermal and dielectric barrier discharge plasma) increased with increasing Fe $_3$ O $_4$  particle size. The turnover frequencies (TOFs) were increased from 0.9 to 5.8 s<sup>-1</sup> with an increasing Fe $_3$ O $_4$  precursor size from 4.2 to 10.4 nm during the thermocatalytic decomposition. A quite similar "particle size effect" was also observed for the plasma catalytic decomposition, although lower TOF was observed. Additionally, reaction-induced catalyst reconstruction was identified during the



early-stage of the catalytic decomposition and can be attributed to the nitridation of  $FeO_x$  to  $Fe_xN$ . Our results provide new evidence for the "structure-sensitivity" of the catalytic  $NH_3$  decomposition.

# ■ INTRODUCTION

Heterogeneous catalysis by nanosized transition metal particles has, frequently, been found to be "structure-sensitive". The specific reaction rates and selectivities are sensitive (either increase or decrease) to the metal particle size, leading to the significant "particle size effect". Therefore, understanding the size-reactivity relationship is critical to the "structure-sensitive" heterogeneous catalytic processes. Various synthesis strategies have been developed for the preparation of nanoparticles with uniform sizes and morphologies, based on which many studies were performed to understand the nature of the size and morphology effect.

An intriguing example of "structure-sensitivity" is identified in the conventional ammonia synthesis (known as the Habor–Bosch process: fixing N<sub>2</sub> and H<sub>2</sub> to produce NH<sub>3</sub><sup>13</sup>), which has been verified by several pioneers in the field of heterogeneous catalysis during the 1970s–1980s. <sup>14</sup> For example, Dumesic and Boudart identified that the turnover frequency (TOF) (referred to as "turnover number" in their original paper) of the small Fe particles is an order of magnitude smaller than that for larger particles. <sup>15</sup> According to Ertl and co-workers, nitrogen adsorption on well-defined Fe single-crystal surfaces demonstrated a strongly anisotropic nature. <sup>16</sup> The Fe(111) plane, due to the presence of exposed seven-coordinated Fe atoms on the surface, has been found to be the most active plane for nitrogen dissociation. <sup>17</sup> The same conclusion was also addressed by Somorjai and co-workers, <sup>18</sup> where an activity ratio of 418:25:1 was found for the Fe(111), Fe(100), and Fe(110) planes, respectively. <sup>18,19</sup> Besides the commercial Fe-

based catalysts, other catalysts, such as  $Mo_2N$ ,  $^{20}$  Re,  $^{21}$  and Ru,  $^{22,23}$  also demonstrated the same "structure-sensitivity". For example, Volpe and Boudart identified that the turnover rates of ammonia synthesis on  $Mo_2N$  decreased by a factor of 25 as the particle size decreased from 12 to 3 nm.  $^{20}$  The Somorjai group found that, for the Rhenium catalyst, the reactivity ratio for the Re(0001), Re(1010), Re(1120), and Re(1121) crystal faces was 1:94:920:2820, respectively.  $^{21}$ 

As the reverse process of ammonia synthesis, ammonia decomposition has recently received increasing attention because NH<sub>3</sub> has been considered a promising H<sub>2</sub> carrier. Ammonia has a high volumetric (121 kg H<sub>2</sub>/m³) and gravimetric (17.75 wt %) hydrogen capacity and can be readily liquefied at a mild pressure of  $\sim$ 8 bar at room temperature, giving rise to an energy density of 4.25 kW h/L. Therefore, NH<sub>3</sub> decomposition has been extensively studied for CO<sub>x</sub>-free H<sub>2</sub> production recently. Quite similar to NH<sub>3</sub> synthesis, the "structure-sensitivity" has also been identified for NH<sub>3</sub> decomposition over the Ni, 30,31 Ir, 32 Ru, 33 and Pt<sup>34</sup> catalysts. With the Ni-based catalysts, the first-principles calculation suggested that the energy barrier of

Received: June 13, 2022 Revised: July 14, 2022 Accepted: July 15, 2022 Published: August 1, 2022





associative desorption of N on the stepped Ni(211) is 1.1 eV higher than that on the closed-packed Ni(111). Ocn-sequently, the turnover rates increased with increasing Ni particle size. Nonetheless, a similar "particle size"/"structure-sensitivity" effect for NH<sub>3</sub> decomposition over the Fe-based catalyst has not been systematically elucidated. Noteworthily, most of the current studies on NH<sub>3</sub> decomposition focus on the thermocatalytic process, which requires a temperature of up to 550 °C. At low temperatures, the recombinative desorption of nitrogen (N<sub>ad</sub>) from the catalyst surface is significantly inhibited. While plasma driven catalysis has been proposed to assist the decomposition of NH<sub>3</sub>, the influence of particle size on the activity has not been studied.

Recently, we developed a continuous growth method to synthesize water-dispersible iron oxide nanoparticles with precisely controlled sizes. <sup>38,39</sup> In this method, the nanoparticles with increasing sizes could be synthesized, under the same reaction conditions (temperature and solvent), by repeatedly adding the reactant for additional growth. The reaction provides ideal nanoparticles to study the size-dependent behavior for the "structure-sensitivity". In this paper, a series of water-dispersible Fe<sub>3</sub>O<sub>4</sub> nanoparticles with narrow size distributions were synthesized and employed as the precursors of Fe<sub>3</sub>O<sub>4</sub>/Al<sub>2</sub>O<sub>3</sub> catalysts to study the size-dependent activity. With Fe<sub>3</sub>O<sub>4</sub> particle sizes of 4.2  $\pm$  0.6, 6.1  $\pm$  0.8, 8.1  $\pm$  1, and  $10.4 \pm 1$  nm prepared, we will demonstrate the influence of particle size on the activity of both thermal and plasma driven catalytic NH<sub>3</sub> decomposition. Specifically, we show that the TOF increases with increasing Fe<sub>3</sub>O<sub>4</sub> particle size. Noteworthily, the Fe<sub>3</sub>O<sub>4</sub> nanoparticles on the Al<sub>2</sub>O<sub>3</sub> support were partially reduced to FeO<sub>x</sub> during activation in H<sub>2</sub> (10%) and transformed into Fe<sub>x</sub>N during the early-stage of the reaction.

#### EXPERIMENTAL SECTION

Synthesis of Fe<sub>3</sub>O<sub>4</sub> Nanoparticles. The iron oxide nanoparticles were synthesized through the polyol method according to our previous studies. 38,39 Typically, iron(III) acetylacetonate (Fe(acac)<sub>3</sub>) (88 mg, 0.25 mmol) was first mixed with diethylene glycols (DEG) (2.5 mL) in a threenecked flask under argon to obtain solution A (0.1 mmol Fe/ mL). In another flask, Fe(acac)<sub>3</sub> (211 mg, 0.6 mmol) was mixed with DEG (6 mL) to obtain solution B (0.1 mmol Fe/ mL). The obtained solutions (A and B) were heated to 120 °C for an hour. Then, solution B was kept at 70 °C for later use. Solution A was further heated slowly (heating rate of 2.5 °C/ min) to the desired temperature for 2 h for the first growth. After that, solution B (2.5 mL, 0.25 mmol) was added to react for another 2 h, as the second growth. The solution B was added repeatedly to synthesize iron oxide nanoparticles with desired sizes. The samples were mixed with MilliQ water and purified by centrifugal filtration (Amicon, 30 K). After being repeated three times, the final products were dispersed in MilliQ water for further use.

**Preparation of Fe**<sub>3</sub>O<sub>4</sub>/Al<sub>2</sub>O<sub>3</sub>. Fe<sub>3</sub>O<sub>4</sub>/Al<sub>2</sub>O<sub>3</sub> catalysts were prepared through impregnation of the as-synthesized Fe<sub>3</sub>O<sub>4</sub> nanoparticles (in aqueous) on the  $\gamma$ -Al<sub>2</sub>O<sub>3</sub> support (Inframat Advanced Materials: Product #26N-0801G), which has an average particle size of 20–50 nm and BET surface area >150 m²/g. Before impregnation, the Al<sub>2</sub>O<sub>3</sub> support was first calcined at 550 °C for 12 h in a muffle furnace. Typically, the appropriate amounts of the as-synthesized Fe<sub>3</sub>O<sub>4</sub> nanoparticles (~5 mg Fe in water) were diluted to around 5 mL and added to 0.5 g of Al<sub>2</sub>O<sub>3</sub>. The obtained slurry was then

sonicated for 10 min before being transferred to a rotary evaporator to remove water under a vacuum of 150 mbar at 65 °C. The obtained sample was dried under air at 100 °C overnight and then calcined at 450 °C for 4 h (to remove trance DEG) in a tube furnace at a ramp of 5 °C/min under 100 mL/min of dry air. The Fe loadings according to the ICP-MS were 0.7, 0.46, 0.46, and 0.35 wt % for the Fe<sub>3</sub>O<sub>4</sub> with particle sizes of 4.2  $\pm$  0.6, 6.1  $\pm$  0.8, 8.1  $\pm$  1, and 10.4  $\pm$  1 nm, respectively.

Catalyst Characterization. Transmission electron microscopy (TEM) images and STEM-EDX chemical mapping of the activated catalysts were obtained using a JEOL 2100TEM (accelerating voltage 200 kV) equipped with a Gatan camera. The diluted sample in isopropanol was cast on FCF300-CU (Electron Microscopy Science) 300 mesh carbon-coated copper grid and allowed to dry at room temperature overnight. The size analysis from TEM images was performed using ImageJ software (version 1.52a) by taking the average size of 100 particles.

The X-ray photoelectron spectroscopy (XPS) analysis was carried out with a Scienta Omicron ESCA 2SR XPS system equipped with a flood source charge neutralizer. The powder samples were pressed into thin pellets, fixed on the sample stage with double-sided carbon tape, and then loaded into the loadlock chamber and pumped until the vacuum was below 5  $\times$  10<sup>-7</sup> mbar before they were transferred into the sample analysis chamber. The XPS spectra were collected with a Mono Al K $\alpha$  X-ray source (1486.6 eV) at a power of 450 W, and the pressure in the analysis chamber was maintained below 5  $\times$  10<sup>-9</sup> mbar. Source and analyzer angle is fixed at 54.7°, and the take-off angle is fixed at 90°. A wide region survey scan and high-resolution core-level scans of all elements of the sample were recorded and calibrated with respect to the C 1s at 284.8 eV.

Thermocatalytic NH<sub>3</sub> Decomposition. The thermocatalytic testing was performed in a "U-shape" quartz reactor [with a volume of 2 mL (id  $\Phi = 1/2''$ )] connected to a home-built gas supply manifold allowing the transient analysis. For all catalytic tests, 0.05 g of the Fe<sub>3</sub>O<sub>4</sub>/Al<sub>2</sub>O<sub>3</sub> catalysts was used. The samples were pre-treated in 10% H<sub>2</sub>/Ar (30 mL/min) at 600 °C (ramp: 10 °C/min) for 1 h. Then, the spectra of pure Ar (30 mL/min) and the mixture of NH<sub>3</sub>/Ar (Ar: 10 mL/min and NH<sub>3</sub>: 20 mL/min) were collected for mass spectrometer calibration by the external standard method. The reactions were performed at 600 °C under atmospheric pressure at a gas hourly space velocity (GHSV) of 600 mL/g/min. The earlystage catalytic performance was obtained by switching the reactor inlet from Ar to NH<sub>3</sub>/Ar, and the back-transient was obtained by switching the influent gas from NH<sub>3</sub>/Ar back to inert (Ar). The reactor effluent was measured by the online Agilent 5973 MS (equipped with MS Sensor 2.0 software, Diablo Analytical, Inc.). The m/z = 16, 28, and 40 for NH<sub>3</sub>, N<sub>2</sub>, and Ar, respectively, were monitored continuously.

**Plasma Catalytic NH<sub>3</sub> Decomposition.** The plasma catalytic testing was performed in a coaxial dielectric barrier discharge (DBD) reactor consisting of a quartz tube with an inner diameter of 4 mm and an outer diameter of 1/4". A scheme of the reactor system is shown in Figure S1a. Specifically, a 6 cm long stainless steel mesh (20 mesh) is employed as the outer electrode and wrapped tight around the quartz tube. A 1/16" tungsten electrode is inserted at the center of the reactor and act as the inner electrode. The discharge volume of the DBD reactor is 0.64 cm<sup>3</sup> without a

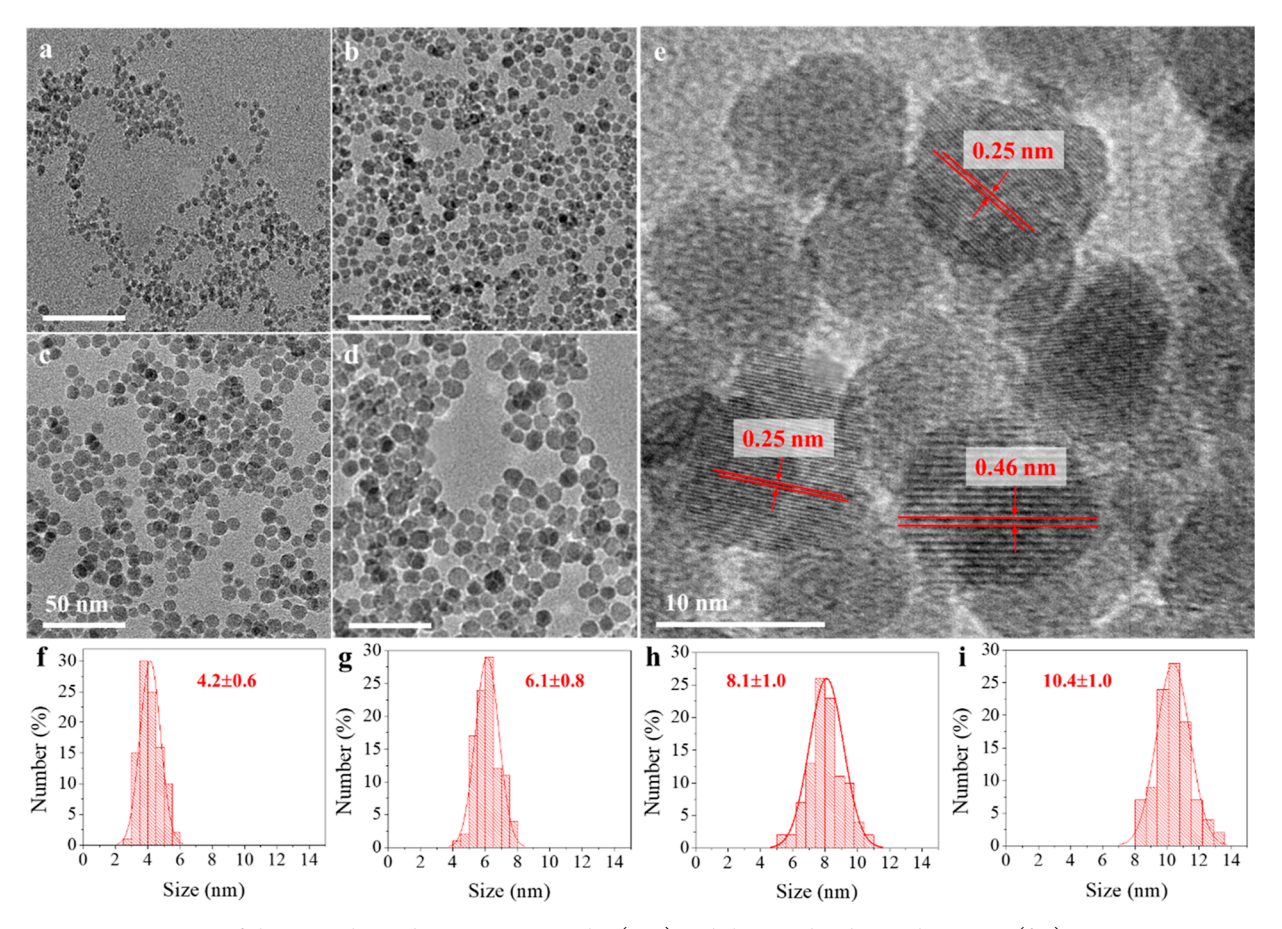


Figure 1. HRTEM images of the as-synthesized Fe<sub>3</sub>O<sub>4</sub> nanoparticles (a-e) and the size distribution histogram (f-i).

catalyst. The DBD plasma was generated using a PMV500 high voltage AC power source with an applied voltage of 10 kV and a frequency of around 24 kHz. The applied voltage was measured using an oscilloscope (Tetronix MDO32 3-BW-100) connected to a high voltage probe (1000:1, Tektronix P6015A), and the gas voltage was measured across a 10 nF capacitor by the same oscilloscope with TPP0250 voltage probe. The power input of the plasma (around 11 W) was measured based on the area inside the charge—voltage (Q-V) Lissajous curves.

During the plasma catalytic testing, a 0.1 g catalyst was loaded into the plasma reactor (see Figure S1b for the details). The reaction was performed under ambient conditions at a total flow rate of 30 mL/min (NH<sub>3</sub> 20 mL/min and Ar 10 mL/min), which provided a specific energy input (SEI) of 22 J/cm<sup>3</sup>. The plasma reactor outlet was measured directly by the same Agilent 5973 MS.

**TOF Evaluation.** The apparent TOF was calculated based on the total surface area per gram of Fe nanoparticles, which can be calculated from

$$S = \frac{6}{\rho \emptyset}$$

where  $\rho$  is the bulk density of Fe (7.89 × 10<sup>6</sup> m<sup>3</sup>/g) and  $\phi$  is the diameter of the particles after catalysis (similar to the Fe<sub>3</sub>O<sub>4</sub> precursor according to the TEM of the used samples).

A surface area of  $0.0613~\text{nm}^2$  per iron atom was used for TOF calculation, corresponding to  $\sim 16~\text{Fe}$  atoms per  $\text{nm}^2$ . The TOF is calculated from

$$TOF = \frac{r \times 6.13 \times 10^{-20} \times N_a}{S}$$

where r is the reaction rate  $(\text{mol}_{\text{NH}_3}/\text{g}_{\text{Fe}}/\text{min})$  and  $N_{\text{a}}$  is the Avogadro constant.

Although the reduced Fe nanoparticles were transformed into Fe<sub>x</sub>N during the reaction, the nitridation decreases simultaneously the bulk density  $\rho$  (increases the total surface area S) and site density (increases the surface area per iron atom). Therefore, estimating the TOF based on Fe could only introduce a negligible error.

#### RESULTS AND DISCUSSION

Design and Synthesis of Fe/Al<sub>2</sub>O<sub>3</sub> Catalysts with **Different Fe Sizes.** The Fe/Al<sub>2</sub>O<sub>3</sub> catalysts (with different Fe sizes ranging from 4-11 nm) employed for NH3 decomposition were prepared using the water-dispersible Fe<sub>3</sub>O<sub>4</sub> nanoparticles as the precursor. The Fe<sub>3</sub>O<sub>4</sub> nanoparticles were introduced into the  $\gamma$ -Al<sub>2</sub>O<sub>3</sub> support through impregnation under sonication using water as the solvent. To obtain waterdispersible Fe<sub>3</sub>O<sub>4</sub> nanoparticles with tunable and narrow size distributions, we employed the polyol method.<sup>38,39</sup> The strategy is based on the thermal decomposition of the Fe(acac)<sub>3</sub> precursor in the DEGs. The particle size was tuned by a stepwise growth. With such a synthesis strategy, four samples of Fe<sub>3</sub>O<sub>4</sub> nanoparticles with different sizes were prepared. The representative TEM images of the Fe<sub>3</sub>O<sub>4</sub> nanoparticles and their corresponding size distribution histogram are shown in Figure 1a-d and f-i, respectively. It is seen that water-dispersible Fe<sub>3</sub>O<sub>4</sub> nanoparticles with sizes of 4.2  $\pm$ 

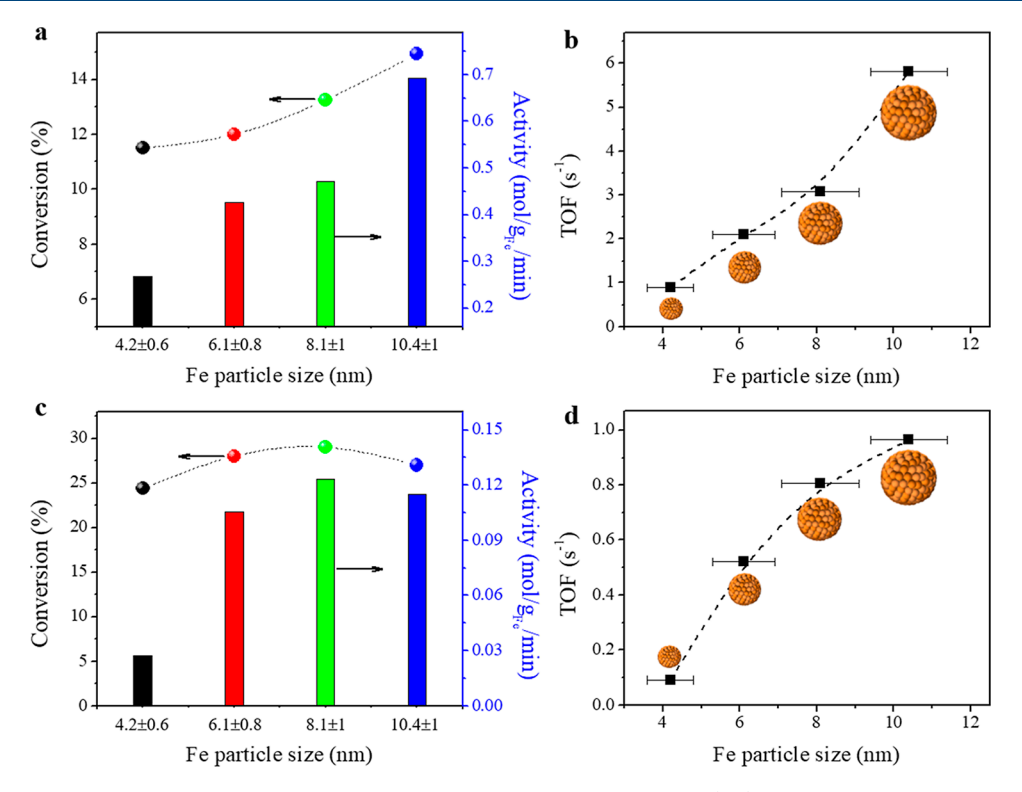


Figure 2. Influence of  $Fe_3O_4$  nanoparticle size on the catalytic activity of  $NH_3$  decomposition. (a,b) Conversion, specific activity, and TOF during the thermocatalytic reaction at 600 °C. (c,d) Conversion, specific activity, and TOF during plasma catalytic reaction without external heating.

0.6, 6.1  $\pm$  0.8, 8.1  $\pm$  1, and 10.4  $\pm$  1 nm were successfully synthesized. Specifically, the Fe<sub>3</sub>O<sub>4</sub> nanoparticles show spheric morphology and quite narrow size distributions (deviation  $\leq 1$ nm statistically). The size and morphology of the nanoparticles on the Al<sub>2</sub>O<sub>3</sub> support are almost unchanged after the reaction (vide infra). The selected high-resolution transmission electron microscopy (HRTEM) image of the nanoparticles is shown in Figure 1e. The measured lattice distance of the majority of the nanoparticles is around 0.25 nm, which corresponds to the (311) plane of the Fe<sub>3</sub>O<sub>4</sub> crystalline phase. The identification of the (311) plane from the HRTEM is consistent with the XRD pattern of the Fe<sub>3</sub>O<sub>4</sub> nanoparticles, <sup>38</sup> where the (311) plane was found to be the most intense diffraction peak (JCPDS no. 03-0863). The measured lattice distance around 0.46 nm was also identified by the HRTEM, which can be assigned to the (111) plane of the Fe<sub>3</sub>O<sub>4</sub> crystalline.

Size-Dependent Activity in Thermocatalytic NH<sub>3</sub> **Decomposition.** The catalytic performance of the Fe<sub>3</sub>O<sub>4</sub>/ Al<sub>2</sub>O<sub>3</sub> catalysts (with different Fe<sub>3</sub>O<sub>4</sub> nanoparticle sizes) in thermocatalytic NH<sub>3</sub> decomposition is shown in Figure 2a,b. As shown in Figure 2a (left axis), during the thermocatalytic NH<sub>3</sub> decomposition at 600 °C, NH<sub>3</sub> conversion between 11.5-15% was obtained over the Fe<sub>3</sub>O<sub>4</sub>/Al<sub>2</sub>O<sub>3</sub> catalysts. It is seen that NH<sub>3</sub> conversion increases with increasing Fe<sub>3</sub>O<sub>4</sub> nanoparticles size. Noteworthily, the Al<sub>2</sub>O<sub>3</sub> used in this study is almost inactive for the thermocatalytic NH<sub>3</sub> decomposition under the investigated conditions (see Figure S2). Therefore, the NH<sub>3</sub> conversion was converted into mass-specific activity (per gram of Fe). As shown in Figure 2a: right axis, the specific activity increased from 0.27 to 0.69  $\text{mol}_{\text{NH}_3}/g_{\text{Fe}}/\text{min}$  with increasing  $\mathrm{Fe_3O_4}$  nanoparticles size from 4.2 to 10.4 nm. The specific activity over the present Fe/Al<sub>2</sub>O<sub>3</sub> catalysts is significantly higher than that of the Fe/CNFs reported in the literature (the activity of the Fe/CNFs catalyst was estimated

to be  $\sim 0.14~{\rm mol_{NH_3}/g_{Fe}/min}).^{35}$  In the literature, the particle size of the Fe species was found to be 40–300 nm. We expect that the present catalysts demonstrated a higher mass-specific activity due to the rationally designed Fe $_3O_4$  nanoparticles at the relatively smaller size range.

The mass-specific activities were further converted into TOFs for a better demonstration of the "particle size effect". TOF values were calculated using simple geometric arguments for spherical particle shapes and a surface iron density of 0.0613 nm<sup>-2</sup> corresponding to ~16 atoms of Fe nm<sup>-2</sup>. 10 It must be noted that the Fe<sub>3</sub>O<sub>4</sub> nanoparticles were partially reduced to FeOx during H2 pre-treatment and converted into Fe, N during the reaction (vide infra), which could lead to TOF values deviation slightly from that obtained based on Fe<sup>0</sup>. The TOF values (see Figure 2b) were increased from 0.9 to  $5.8 \text{ s}^{-1}$  with an increasing Fe<sub>3</sub>O<sub>4</sub> nanoparticles size from 4.2 to 10.4 nm. We expect that the TOF could further increase with increasing Fe<sub>3</sub>O<sub>4</sub> nanoparticle size. For example, the TOF estimated from the literature<sup>35</sup> is around 9 s<sup>-1</sup> when the average particle size is around 100 nm. Nonetheless, the massspecific activity must be decreased at a larger particle size due to the loss of total metal surface area per gram of nanoparticles.

**Size-Dependent Activity in Plasma Catalytic NH<sub>3</sub> Decomposition.** The integration of DBD non-thermal plasma (NTP) with heterogeneous catalytic processes is an emerging technology for low-temperature chemical transformations. Therefore, unlike the thermocatalytic NH<sub>3</sub> decomposition which requires a reaction temperature up to 600 °C, the plasma catalytic reaction was performed under "ambient conditions" (without external heat supply). The temperature of the reactor is around 200 °C (measured by attaching a thermocouple to the outer electrode right after the shutdown of plasma) with the applied power of plasma. The electrical signals of the applied discharge in the mixing of NH<sub>3</sub>

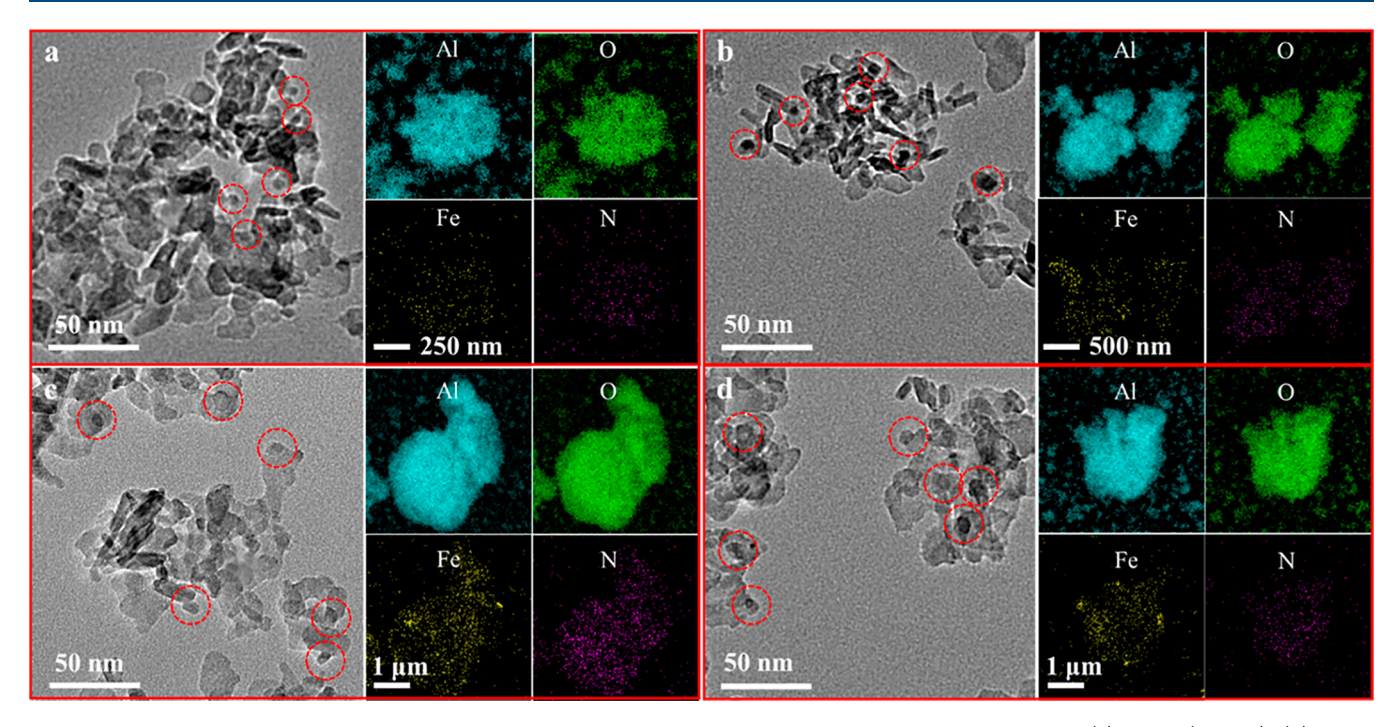


Figure 3. TEM and STEM-EDS images of the  $Fe_3O_4/Al_2O_3$  catalysts after NH<sub>3</sub> decomposition at 600 °C for 1 h. (a)  $Fe_3O_4$  (4.2 nm), (b)  $Fe_3O_4$  (6.1 nm), (c)  $Fe_3O_4$  (8.1 nm), and (d)  $Fe_3O_4$  (10.4 nm).

and Ar with  ${\rm Fe/Al_2O_3}$  catalyst are shown in Figure S3a, and the  $Q{-}V$  Lissajous curve of the discharge is shown in Figure S3b. It is seen that the shape of the Lissajous curve is between a parallelogram and oval shape, which is a typical discharge behavior in the presence of catalytic material. The power deposition from the applied voltage was calculated based on the area of the Lissajous curve, and it is 11 W.

The activity of plasma driven  $NH_3$  decomposition in terms of conversion, specific activities, and TOF is shown in Figures 2c,d and S4. Unlike the thermocatalytic reaction, during which  $NH_3$  decomposition is negligible over the  $Al_2O_3$ , as shown in Figure S4, the conversion of  $NH_3$  is around 15% without a catalyst (plasma alone) and 22% when packed with  $Al_2O_3$ . Ammonia conversion increased from 22% to a range between 24–29% with the presence of  $Fe_3O_4$  nanoparticles with different sizes. The space-time activity ranges from 200-240  $\mu$ mol/min, which corresponds to the plasma efficiency of 0.3-0.36 mmol $_{NH_3}/kJ_{plasma}$ . Note that  $NH_3$  conversion/activity over the  $Fe_3O_4/Al_2O_3$  catalyst increased with increasing  $Fe_3O_4$  particle size from 4.2 to 8.1 nm, which is quite similar to the thermocatalytic reaction. However,  $NH_3$  conversion/activity decreased with a further increase of the  $Fe_3O_4$  size from 8.1 to 10.4 nm.

Considering that the  $Al_2O_3$ -packed plasma reactor shows considerable activity in  $NH_3$  decomposition, the activity attained on the  $Fe_3O_4$  nanoparticles was deconvoluted from the overall activity by subtracting the activity of the plasma packed with  $Al_2O_3$ . As shown in Figure 2c, the mass-specific activity over the Fe nanoparticles ranges from 0.03-0.12  $mol_{NH_3}/g_{Fe}/min$ , which is about an order of magnitude lower than the thermocatalytic reactions. The same as  $NH_3$  conversion, the mass-specific activity increased with increasing  $Fe_3O_4$  size from 4.2 to 8.1 nm but decreased with further increasing the size to 10.4 nm. Nevertheless, the TOF values (see Figure 2d) were continuously increased from 0.09 to 0.96

 $s^{-1}$  with an increasing  $Fe_3O_4$  nanoparticle size from 4.2 to 10.4 nm

**Discussion.** The above results demonstrate a significant "particle size effect" in NH3 decomposition, driven by both heat and DBD plasma, over the Fe<sub>3</sub>O<sub>4</sub>/Al<sub>2</sub>O<sub>3</sub> catalyst. Generally, the TOF increases with increasing Fe<sub>3</sub>O<sub>4</sub> particle size, which is quite similar to the trend observed by Boudart and co-workers in NH3 synthesis over the Fe and Mo2N catalysts. 15,20 Therefore, it might be expected that the relative proportion of sites that have higher activity for NH3 decomposition would decrease as particle size becomes smaller. 15 Further information about the catalytically active phase will be discussed based on the characterization of the used catalyst as well as the kinetic behavior during the transient experiment. The TEM images and STEM-EDS mappings of the Fe<sub>3</sub>O<sub>4</sub>/Al<sub>2</sub>O<sub>3</sub> catalysts after thermocatalytic NH<sub>3</sub> decomposition are shown in Figure 3. It is seen from the TEM images that the size of the nanoparticles (highlighted with red circles) was almost not changed after being impregnated to the Al<sub>2</sub>O<sub>3</sub> support and subjected to the NH3 decomposition. Note that the Fe nanoparticles cannot be clearly distinguished from the Al<sub>2</sub>O<sub>3</sub> support from the TEM images, which is not a surprise due to the low loading. Nonetheless, from the STEM-EDS mapping, the Fe species were found to distribute among the  $Al_2O_3$  support.

Another piece of important information from the STEM–EDS is the N mapping. It is seen that N is distributed homogeneously with Fe for all of the four catalysts after NH<sub>3</sub> decomposition, indicating that the Fe<sub>3</sub>O<sub>4</sub> nanoparticles were transformed into iron nitride (Fe<sub>x</sub>N) during the reaction. The formation of Fe<sub>x</sub>N was also verified by the XPS spectra of the Fe<sub>3</sub>O<sub>4</sub>/Al<sub>2</sub>O<sub>3</sub> catalyst after catalysis. As shown in Figure 4, a clear peak of N 1s was observed for all of the used catalysts, which suggested the occurrence of surface nitridation during the NH<sub>3</sub> decomposition. However, the Fe 2p peaks of the fresh and used catalysts reveal a feature dominated by iron oxides at

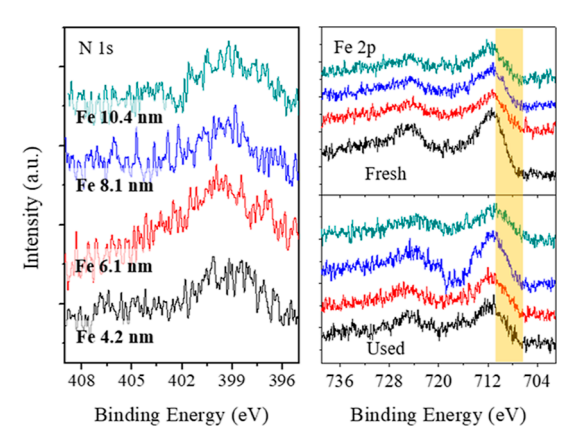
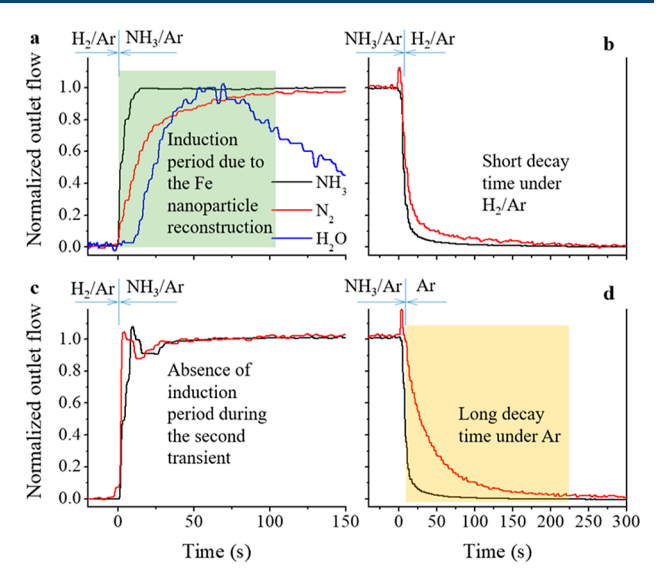


Figure 4. XPS spectra of  $Fe/Al_2O_3$  catalysts with different Fe particle sizes.

a binding energy of 711.5 eV for Fe 2p 3/2 and 724.6 eV for Fe 2p 1/2, indicating that the samples were oxidized during exposure to air. Nonetheless, the peaks of Fe 2p 3/2 for the used catalyst seem broader than the fresh samples, indicating a new peak (at a binding energy of 708 eV for  $Fe_xN^{41}$ ) might be deconvoluted [see Figure S5 for the deconvolution of  $Fe_3O_4$  (4.2 nm)/Al<sub>2</sub>O<sub>3</sub>]. It is seen that while the peak at 708 eV can be deconvoluted for the used  $Fe_3O_4$  (4.2 nm)/Al<sub>2</sub>O<sub>3</sub> catalyst, such a peak was absent for the fresh catalyst. Therefore, the Fe 2p XPS spectra once again suggested the presence of the  $Fe_xN$  phase, which can be oxidized when exposed to air.

Indeed, the formation of iron nitride was not a surprise during the NH<sub>3</sub> decomposition because of the high N-N recombination barrier (which favors the nitridation). Back to the early work by Boudart and co-workers, a complete transformation of the metallic iron particles into iron nitride was realized at 670 K under NH<sub>3</sub>. Therefore, the actual working catalyst for the NH<sub>3</sub> decomposition must be Fe<sub>x</sub>N, although deep nitridation has been found to deactivate the catalyst. According to recent work by Lu et al., the highest NH<sub>3</sub> decomposition activity was observed over the Fe/Fe<sub>4</sub>N mixing phase. The authors suggested that the deposition of an N on the Fe(100) surface modifies the electronic structure of its surrounding iron atoms, causing a significant reduction of the initial dehydrogenation barrier of NH<sub>3</sub>.

The nitridation of FeO<sub>x</sub> nanoparticles during the NH<sub>3</sub> decomposition can be further discussed based on the chemical transient analysis. As shown in Figure 5a, during the early-stage of the NH<sub>3</sub> decomposition, N<sub>2</sub> takes a significantly longer time (>100 s) to reach the steady-state than NH<sub>3</sub> (<15 s). However, such a delay (in reaching the steady-state) was absent during the second circle early-stage (see Figure 5c). Therefore, the results indicated the occurrence of significant reconstruction of the catalytically active sites during the first circle of the transient analysis. Such a reconstruction, according to the XPS and STEM-EDS characterization discussed above, must be associated with the nitridation of the FeO<sub>x</sub> nanoparticles. Additionally, a pronounced peak of H2O was observed during the first circle early-stage transient, indicating that the Fe<sub>3</sub>O<sub>4</sub> nanoparticles were partially reduced to FeO, during the H2 pre-treatment. After the reaction reaches steady-state, the reactor inlet was switched from NH<sub>3</sub>/Ar back to H<sub>2</sub>/Ar or Ar, leading to the back-transient behavior of such a catalytic system (see Figure 5b,d). The decay time of  $N_2$  is significantly longer under Ar than that in 10% H<sub>2</sub>/Ar, indicating that the



**Figure 5.** Transient analysis of thermocatalytic  $NH_3$  decomposition over the  $Fe_3O_4/Al_2O_3$  catalyst. (a) Early-stage catalytic behavior after switching the reactor inlet from  $H_2/Ar$  to  $NH_3/Ar$ ; (b) back-transient behavior after switching from  $NH_3/Ar$  back to  $H_2/Ar$ ; (c) second circle early-stage behavior; and (d) back-transient behavior after switching from  $NH_3/Ar$  to Ar.

presence of  $H_2$  facilitates the N-N recombination and desorption. With the presence of  $H_2$ ,  $Fe_xN$  can be reduced back to the elemental Fe, consequently, favoring the desorption of the residual  $N_{ads}$ . According to Ganley et al., <sup>45</sup> the NH<sub>3</sub> decomposition rate over the Fe is limited by the N-N recombination  $(2N_{(ads)} \rightarrow N_{2(g)})$ .

From a practical point of view, the present study compared the activity of NH<sub>3</sub> decomposition driven by both thermal and DBD plasma. While the thermocatalytic decomposition shows higher TOF, the space-time yield of the present model catalysts remains low due to the lower Fe loading. The plasmaassisted NH<sub>3</sub> decomposition, although showing significantly higher overall activity under "ambient conditions" (without external heat supply), the plasma/catalyst synergy needs to be further optimized in order to increase the energy efficiency. Specifically, the energy efficiency of the plasma during the present study is 1.5-2 mol<sub>H</sub>,/kW h, quite similar to that reported by Wang et al. for the plasma NH3 decomposition over the Fe-based catalyst.<sup>37</sup> We expect that the energy efficiency of the plasma catalytic decomposition can be enhanced by increasing the Fe loading, optimizing the ratio between the volumes of plasma to catalysts, and electrode materials, as well as the plasma catalytic reactor optimization. For example, an adiabatic plasma reactor (minimizing the heat loss to the surrounding) could significantly increase the efficiency (results are not shown), because the NH<sub>3</sub> decomposition is an endothermic reaction.

#### CONCLUSIONS

We demonstrated the presence of the pronounced "particle size effect" in  $NH_3$  decomposition over the  $Fe_3O_4/Al_2O_3$  catalyst and compared the size-dependent activity between the thermocatalytic decomposition and the DBD plasma-assisted decomposition. We synthesized the water-dispersible with narrow size distribution  $Fe_3O_4$  nanoparticles with diameters between 4–11 nm through thermal decomposition of  $Fe(acac)_3$  in the DEGs. Then, the  $Fe_3O_4/Al_2O_3$  model

catalysts with different particle sizes were prepared using the as-synthesized Fe<sub>3</sub>O<sub>4</sub> as the precursor. Specifically, the TOF values for the thermal and plasma driven catalytic NH3 decomposition showed the same trend, namely, the TOF value increases with increasing  $Fe_3O_4$  particle size. The TOF was increased from 0.9 to 5.8 s<sup>-1</sup> (during the thermocatalytic decomposition) and from 0.09 to 0.96 s<sup>-1</sup> (during the plasma driven decomposition) with the increase of Fe<sub>3</sub>O<sub>4</sub> size from 4.2 to 10.4 nm. We also identified the reaction-induction reconstruction during the early-stage of the thermocatalytic decomposition, which can be attributed to the nitridation of FeO<sub>x</sub> to Fe<sub>x</sub>N. Such a reconstruction of the catalytically active phase under the reaction conditions has been widely studied for the Fe catalysts during ammonia synthesis and decomposition reactions. The pronounced "particle size effect" demonstrated in this study provided new evidence for the "structure-sensitivity" of the catalytic NH<sub>3</sub> decomposition.

#### ASSOCIATED CONTENT

# Supporting Information

The Supporting Information is available free of charge at https://pubs.acs.org/doi/10.1021/acs.iecr.2c02092.

Experimental setup for plasma catalytic reaction, electrical signals of plasma, and additional catalytic data (PDF)

## AUTHOR INFORMATION

#### **Corresponding Authors**

Yongfeng Zhao — Department of Chemistry, Physics and Atmospheric Science, Jackson State University, Jackson, Mississippi 39217, United States; orcid.org/0000-0003-2962-7504; Email: yongfeng.zhao@jsums.edu

#### **Authors**

Genwei Chen – Dave C. Swalm School of Chemical Engineering, Mississippi State University, Mississippi State, Mississippi 39762, United States

Jing Qu — Department of Chemistry, Physics and Atmospheric Science, Jackson State University, Jackson, Mississippi 39217, United States

Pohlee Cheah – Department of Chemistry, Physics and Atmospheric Science, Jackson State University, Jackson, Mississippi 39217, United States

Dongmei Cao – Material Characterization Center, Louisiana State University, Baton Rouge, Louisiana 70803, United States

Complete contact information is available at: https://pubs.acs.org/10.1021/acs.iecr.2c02092

# **Author Contributions**

G.C. and J.Q. contributed equally to the experimental work described in this paper.

#### Notes

The authors declare no competing financial interest.

#### ACKNOWLEDGMENTS

This work is partially supported by National Science Foundation (DMR-2000135). Y.X. gratefully acknowledges

the TEM work [supported by the National Science Foundation (no. MRI-1126743)] at the Institute for Imaging and Analytical Technologies (I2AT) at Mississippi State University.

# REFERENCES

- (1) Carberry, J. J. Structure sensitivity in heterogeneous catalysis: Activity and yield/selectivity. *J. Catal.* **1988**, *114*, 277–283.
- (2) Boudart, M. Turnover Rates in Heterogeneous Catalysis. *Chem. Rev.* 1995, 95, 661–666.
- (3) Boudart, M. Heterogeneous catalysis by metals. *J. Mol. Catal.* **1985**, 30, 27–38.
- (4) Bond, G. C. The origins of particle size effects in heterogeneous catalysis. *Surf. Sci.* **1985**, *156*, 966–981.
- (5) Coq, B.; Figueras, F. Structure—activity relationships in catalysis by metals: some aspects of particle size, bimetallic and supports effects. *Coord. Chem. Rev.* **1998**, *178*–*180*, 1753–1783.
- (6) Zhu, J.; Zhang, G.; Li, W.; Zhang, X.; Ding, F.; Song, C.; Guo, X. Deconvolution of the Particle Size Effect on CO<sub>2</sub> Hydrogenation over Iron-Based Catalysts. ACS Catal. **2020**, *10*, 7424–7433.
- (7) Bezemer, G. L.; Bitter, J. H.; Kuipers, H. P. C. E.; Oosterbeek, H.; Holewijn, J. E.; Xu, X.; Kapteijn, F.; van Dillen, A. J.; de Jong, K. P. Cobalt Particle Size Effects in the Fischer—Tropsch Reaction Studied with Carbon Nanofiber Supported Catalysts. *J. Am. Chem. Soc.* 2006, 128, 3956—3964.
- (8) den Breejen, J. P.; Radstake, P. B.; Bezemer, G. L.; Bitter, J. H.; Frøseth, V.; Holmen, A.; de Jong, K. P. d. On the Origin of the Cobalt Particle Size Effects in Fischer—Tropsch Catalysis. *J. Am. Chem. Soc.* **2009**, *131*, 7197—7203.
- (9) Kuhn, J. N.; Huang, W.; Tsung, C.-K.; Zhang, Y.; Somorjai, G. A. Structure Sensitivity of Carbon—Nitrogen Ring Opening: Impact of Platinum Particle Size from below 1 to 5 nm upon Pyrrole Hydrogenation Product Selectivity over Monodisperse Platinum Nanoparticles Loaded onto Mesoporous Silica. *J. Am. Chem. Soc.* **2008**, *130*, 14026—14027.
- (10) Iablokov, V.; Xiang, Y. Z.; Meffre, A.; Fazzini, P. F.; Chaudret, B.; Kruse, N. Size-Dependent Activity and Selectivity of Fe/MCF-17 in the Catalytic Hydrogenation of Carbon Monoxide Using Fe(0) Nanoparticles as Precursors. ACS Catal. 2016, 6, 2496–2500.
- (11) Jamkhande, P. G.; Ghule, N. W.; Bamer, A. H.; Kalaskar, M. G. Metal nanoparticles synthesis: An overview on methods of preparation, advantages and disadvantages, and applications. *J. Drug Deliv. Sci. Technol.* **2019**, 53, 101174.
- (12) Quinson, J.; Inaba, M.; Neumann, S.; Swane, A. A.; Bucher, J.; Simonsen, S. B.; Theil Kuhn, L.; Kirkensgaard, J. J. K.; Jensen, K. M. Ø.; Oezaslan, M.; Kunz, S.; Arenz, M. Investigating Particle Size Effects in Catalysis by Applying a Size-Controlled and Surfactant-Free Synthesis of Colloidal Nanoparticles in Alkaline Ethylene Glycol: Case Study of the Oxygen Reduction Reaction on Pt. ACS Catal. 2018, 8, 6627–6635.
- (13) Liu, H. Ammonia synthesis catalyst 100 years: Practice, enlightenment and challenge. Chin. J. Catal. 2014, 35, 1619–1640.
- (14) Parker, I. B.; Waugh, K. C.; Bowker, M. On the structure sensitivity of ammonia synthesis on promoted and unpromoted iron. *J. Catal.* **1988**, *114*, 457–459.
- (15) Dumesic, J. A.; Topsøe, H.; Khammouma, S.; Boudart, M. Surface, catalytic and magnetic properties of small iron particles: II. Structure sensitivity of ammonia synthesis. *J. Catal.* **1975**, *37*, 503–512
- (16) Ertl, G.; Lee, S. B.; Weiss, M. Kinetics of nitrogen adsorption on Fe(111). Surf. Sci. 1982, 114, 515–526.
- (17) Ertl, G. Surface Science and Catalysis—Studies on the Mechanism of Ammonia Synthesis: The P. H. Emmett Award Address. Catal. Rev.—Sci. Eng. 1980, 21, 201–223.
- (18) Spencer, N. D.; Schoonmaker, R. C.; Somorjai, G. A. Structure sensitivity in the iron single-crystal catalysed synthesis of ammonia. *Nature* **1981**, *294*, 643–644.

- (19) Spencer, N. D.; Schoonmaker, R. C.; Somorjai, G. A. Iron single crystals as ammonia synthesis catalysts: Effect of surface structure on catalyst activity. J. Catal. 1982, 74, 129-135.
- (20) Volpe, L.; Boudart, M. Ammonia synthesis on molybdenum nitride. J. Phys. Chem. 1986, 90, 4874-4877.
- (21) Asscher, M.; Carrazza, J.; Khan, M. M.; Lewis, K. B.; Somorjai, G. A. The ammonia synthesis over rhenium single-crystal catalysts: Kinetics, structure sensitivity, and effect of potassium and oxygen. J. Catal. 1986, 98, 277-287.
- (22) Rarogpilecka, W.; Miskiewicz, E.; Szmigiel, D.; Kowalczyk, Z. Structure sensitivity of ammonia synthesis over promoted ruthenium catalysts supported on graphitised carbon. J. Catal. 2005, 231, 11-19.
- (23) Li, L.; Jiang, Y.-F.; Zhang, T.; Cai, H.; Zhou, Y.; Lin, B.; Lin, X.; Zheng, Y.; Zheng, L.; Wang, X.; Xu, C.-Q.; Au, C.-t.; Jiang, L.; Li, J. Size sensitivity of supported Ru catalysts for ammonia synthesis: From nanoparticles to subnanometric clusters and atomic clusters. Chem **2022**, 8, 749-768.
- (24) Chen, J. G.; Crooks, R. M.; Seefeldt, L. C.; Bren, K. L.; Bullock, R. M.; Darensbourg, M. Y.; Holland, P. L.; Hoffman, B.; Janik, M. J.; Jones, A. K.; Kanatzidis, M. G.; King, P.; Lancaster, K. M.; Lymar, S. V.; Pfromm, P.; Schneider, W. F.; Schrock, R. R. Beyond fossil fueldriven nitrogen transformations. Science 2018, 360, No. eaar6611.
- (25) Ogasawara, K.; Nakao, T.; Kishida, K.; Ye, T.-N.; Lu, Y.; Abe, H.; Niwa, Y.; Sasase, M.; Kitano, M.; Hosono, H. Ammonia Decomposition over CaNH-Supported Ni Catalysts via an NH<sub>2</sub><sup>-</sup>-Vacancy-Mediated Mars-van Krevelen Mechanism. ACS Catal. 2021,
- (26) Xie, P.; Yao, Y.; Huang, Z.; Liu, Z.; Zhang, J.; Li, T.; Wang, G.; Shahbazian-Yassar, R.; Hu, L.; Wang, C. Highly efficient decomposition of ammonia using high-entropy alloy catalysts. Nat. Commun. 2019, 10, 4011.
- (27) Jolaoso, L.; Zaman, S. F. Catalytic Ammonia Decomposition for Hydrogen Production: Utilization of Ammonia in a Fuel Cell In Sustainable Ammonia Production; Inamuddin, Boddula, R., Asiri, A. M., Eds.; Springer International Publishing: Cham, 2020, pp 81-105.
- (28) Cha, J.; Lee, T.; Lee, Y.-J.; Jeong, H.; Jo, Y. S.; Kim, Y.; Nam, S. W.; Han, J.; Lee, K. B.; Yoon, C. W.; Sohn, H. Highly monodisperse sub-nanometer and nanometer Ru particles confined in alkaliexchanged zeolite Y for ammonia decomposition. Appl. Catal., B 2021, 283, 119627.
- (29) Lucentini, I.; Garcia, X.; Vendrell, X.; Llorca, J. Review of the Decomposition of Ammonia to Generate Hydrogen. Ind. Eng. Chem. Res. 2021, 60, 18560-18611.
- (30) Duan, X.; Qian, G.; Liu, Y.; Ji, J.; Zhou, X.; Chen, D.; Yuan, W. Structure sensitivity of ammonia decomposition over Ni catalysts: A computational and experimental study. Fuel Process. Technol. 2013, 108, 112-117.
- (31) Zhang, J.; Xu, H.; Li, W. Kinetic study of NH<sub>3</sub> decomposition over Ni nanoparticles: The role of La promoter, structure sensitivity and compensation effect. Appl. Catal., A 2005, 296, 257-267.
- (32) Chen, W.; Ermanoski, I.; Madey, T. E. Decomposition of Ammonia and Hydrogen on Ir Surfaces: Structure Sensitivity and Nanometer-Scale Size Effects. J. Am. Chem. Soc. 2005, 127, 5014-
- (33) Lu, X.; Zhang, J.; Chen, W.-K.; Roldan, A. Kinetic and mechanistic analysis of NH<sub>3</sub> decomposition on Ru(0001), Ru(111) and Ir(111) surfaces. Nanoscale Adv. 2021, 3, 1624-1632.
- (34) Gohndrone, J. M.; Olsen, C. W.; Backman, A. L.; Gow, T. R.; Yagasaki, E.; Masel, R. I. Ammonia adsorption and decomposition on several faces of platinum. J. Vac. Sci. Technol., A 1989, 7, 1986-1990.
- (35) Duan, X.; Qian, G.; Zhou, X.; Sui, Z.; Chen, D.; Yuan, W. Tuning the size and shape of Fe nanoparticles on carbon nanofibers for catalytic ammonia decomposition. Appl. Catal., B 2011, 101, 189-
- (36) Schüth, F.; Palkovits, R.; Schlögl, R.; Su, D. S. Ammonia as a possible element in an energy infrastructure: catalysts for ammonia decomposition. Energy Environ. Sci. 2012, 5, 6278-6289.

- (37) Wang, L.; Zhao, Y.; Liu, C.; Gong, W.; Guo, H. Plasma driven ammonia decomposition on a Fe-catalyst: eliminating surface nitrogen poisoning. Chem. Commun. 2013, 49, 3787-3789.
- (38) Cheah, P.; Brown, P.; Qu, J.; Tian, B.; Patton, D. L.; Zhao, Y. Versatile Surface Functionalization of Water-Dispersible Iron Oxide Nanoparticles with Precisely Controlled Sizes. Langmuir 2021, 37, 1279-1287.
- (39) Cheah, P.; Qu, J.; Li, Y.; Cao, D.; Zhu, X.; Zhao, Y. The key role of reaction temperature on a polyol synthesis of water-dispersible iron oxide nanoparticles. J. Magn. Magn. Mater. 2021, 540, 168481.
- (40) Tu, X.; Gallon, H. J.; Twigg, M. V.; Gorry, P. A.; Whitehead, J. C. Dry reforming of methane over a Ni/Al<sub>2</sub>O<sub>3</sub> catalyst in a coaxial dielectric barrier discharge reactor. J. Phys. D: Appl. Phys. 2011, 44, 274007.
- (41) Li, Z.; Tang, G.; Ma, X.; Sun, M.; Wang, L. XPS Study on Chemical State and Phase Structure of PBII Nitriding M50 Steel. IEEE Trans. Plasma Sci. 2010, 38, 3079-3082.
- (42) Wood, T. J.; Makepeace, J. W.; David, W. I. F. Neutron diffraction and gravimetric study of the iron nitriding reaction under ammonia decomposition conditions. Phys. Chem. Chem. Phys. 2017, 19, 27859-27865.
- (43) Lu, B.; Li, L.; Ren, M.; Liu, Y.; Zhang, Y.; Xu, X.; Wang, X.; Qiu, H. Ammonia decomposition over iron-based catalyst: Exploring the hidden active phase. Appl. Catal., B 2022, 314, 121475.
- (44) Arabczyk, W.; Pelka, R. Studies of the Kinetics of Two Parallel Reactions: Ammonia Decomposition and Nitriding of Iron Catalyst. J. Phys. Chem. A 2009, 113, 411-416.
- (45) Ganley, J. C.; Thomas, F. S.; Seebauer, E. G.; Masel, R. I. A Priori Catalytic Activity Correlations: The Difficult Case of Hydrogen Production from Ammonia. Catal. Lett. 2004, 96, 117-122.

# **□** Recommended by ACS

# Ball-Milled Processed, Selective Fe/h-BN Nanocatalysts for CO, Hydrogenation

Denis Leybo, Dmitry V. Shtansky, et al.

NOVEMBER 04 2022

ACS APPLIED NANO MATERIALS

READ 2

## **Induction Heating of Magnetically Susceptible Nanoparticles** for Enhanced Hydrogenation of Oleic Acid

Cameron L. Roman, James A. Dorman, et al.

FEBRUARY 17, 2022

ACS APPLIED NANO MATERIALS

READ **C** 

# Elucidating the Active-Phase Evolution of Fe-Based Catalysts during Isobutane Dehydrogenation with and without CO, in **Feed Gas**

Jiapei Wang, Xiangxue Zhu, et al.

MAY 04, 2022

ACS CATALYSIS

RFAD 17

## Metallic Iron Nanocatalysts for the Selective Acetylene **Hydrogenation under Industrial Front-End Conditions**

Sebastian Hock, Marcus Rose, et al.

DECEMBER 03 2021

ACS SUSTAINABLE CHEMISTRY & ENGINEERING

READ

Get More Suggestions >